A Green's Function Sensor Fusion Approach for Evaluating Spacecraft Entry Heating from On-Board Thermal Instrumentation

Kenneth McAfee[1], Peter B. Sunderland[2], and Oded Rabin[3]
University of Maryland, College Park, MD 20742

Hannah S. Alpert[4]
NASA Ames Research Center, Moffett Field, CA 94035

Measurements of the heat loads experienced by atmospheric entry spacecraft are critical to evaluate the performance of thermal protection systems (TPS), investigate aerothermal phenomena, and validate computational models. Recent space exploration missions have flown both heat flux and temperature sensors embedded in the TPS to measure surface heating values, either directly (via heat flux sensors) or indirectly (via temperature sensors). While heat flux sensors can provide a direct transduction of the surface heat flux, their application in convective environments requires the use of correction factors to recover hot-wall TPS heat flux values from the cold-wall sensor measurement. These correction factors are calculated using computationally inefficient time-marching methods that rely on estimated atmospheric entry parameters. In this paper, a hot-wall heat flux reconstruction algorithm is developed to recover TPS surface heating values directly from collocated heat flux and temperature sensor instrumentation via an inverse heat transfer formulation. The algorithm leverages Green's functions to efficiently model the heat conduction within the heat flux sensor and surrounding TPS and stabilizes the recovery of hot-wall heat flux values using the direct heat flux sensor as a regularization mechanism. The reconstruction framework is applied on 1D and 3D computational model systems to verify the accuracy of the approach and evaluate its sensitivity to varying input parameters. In a variety of heating scenarios, the algorithm can resolve both steady and fast-changing features in the surface heat flux, even in the presence of measurement noise. Compared with a conventional regularization approach, the reconstruction algorithm described herein demonstrates a significant robustness to sub-optimal choice of the user input regularization parameter and better resolves important features in the surface heat flux profile, such as the magnitude and temporal location of peak heating. These results demonstrate the viability of Green's functions to model heat conduction in highly insulating TPS systems and establish the use of a surrogate measurement to stabilize the solution as a promising tool for inverse heat transfer problems.

I. Nomenclature

A, B	=	Cole-Hopf transformation constants
C, C_0	=	proportionality constants between hot- and cold-wall heat flux values
C_p	=	specific heat $\left(J/(kg \cdot K)\right)$

---

[1]Graduate Student, Department of Aerospace Engineering, Student Member AIAA
[2]Professor, Department of Fire Protection Engineering
[3]Associate Professor, Department of Materials Science and Engineering, Institute for Research in Electronics and Applied Physics
[4]Systems Engineer, Entry Systems and Vehicle Development Branch

C_λ	=	proportionality constant between λ_2 and $\lambda_2^{(0)}$
$f(\theta)$	=	Cole-Hopf transformation
$g(\boldsymbol{x}, t)$	=	internal source term (W/m^3)
$g'(\boldsymbol{x}, t)$	=	modified internal source term (W/m^3)
G	=	Green's function $(1/m^3)$
k	=	thermal conductivity $\left(W/(m \cdot K)\right)$
L	=	thickness (m)
L_2	=	2nd derivative finite difference operator
M, N	=	basis function order
$\hat{n}$	=	surface normal vector
N_s	=	number of sampled measurements
q	=	heat flux (W/m^2)
$\boldsymbol{x}$	=	general position coordinates (m)
$\boldsymbol{x_0}$	=	dummy position coordinates (m)
$\boldsymbol{x_T}$	=	temperature probe coordinates (m)
$\boldsymbol{x_{HFS}}$	=	heat flux sensor coordinates (m)
S	=	surface (m^2)
dS_0	=	differential surface element in dummy coordinates
$\tilde{T}$	=	absolute temperature $(°C)$
T	=	temperature relative to initial conditions or a reference temperature $(°C)$
t	=	time (s)
V	=	volume (m^3)
dV_0	=	differential volume integral in dummy coordinates
τ	=	dummy time variable (s)
τ_{HFS}	=	heat flux sensor response time (s)
α	=	thermal diffusivity (m^2/s)
δ	=	Dirac delta function $\left(1/(m^3 \cdot s)\right)$
ϵ	=	integrated effects of temperature-dependent material properties $(°C)$
γ	=	integrated effects of measured quantities $(°C)$
λ	=	Tikhonov regularization coefficient
$\lambda_2, \lambda_2^{(0)}$	=	regularization coefficient for C and C_0
Λ	=	Eigenvalues
ϕ	=	Eigenfunctions
ψ	=	Eigenvectors
ρ	=	density (kg/m^3)
θ	=	transformed temperature
σ	=	standard deviation of measurement noise
χ, μ, ν	=	basis functions
∇	=	gradient operator
∇^2	=	Laplacian operator

II.   Introduction

Embedded thermal measurements are critical to enable the evaluation of heat loads on spacecraft thermal protection systems (TPS) and the near-surface aeroheating environment during atmospheric entry. In recent space exploration missions, heat flux sensors were embedded within the backshell and forebody TPS alongside conventional temperature sensors to measure atmospheric entry heat rates [1–3]. While heat flux sensors provide a direct transduction of the heat flux near the surface of the spacecraft, the interpretation of these measurements in unsteady, convective environments requires a correction factor to account for local heating augmentations at the heat flux sensor surface [2]. Current efforts to estimate cold-wall correction factors, and thus recover the hot-wall TPS heat flux, rely on time-marching computational fluid dynamics (CFD) simulations. Simulation-based cold-wall correction methods are susceptible to large uncertainties, however, as they require estimations of vehicle trajectory, gas kinetics, wall catalysis models, and other flight conditions as input parameters [2,4]. In addition, time-marching-based methods are generally computationally expensive and cannot efficiently survey all possible entry scenarios, exacerbating the uncertainty of the recovered hot-wall heat flux.

Inverse heat transfer (IHT) techniques using TPS-embedded temperature measurement instrumentation can recover surface heat flux values which may better represent the thermal loads on the TPS experienced by entry spacecraft [5,6]. While not a direct measurement of the surface heat flux, these methods have been used to recover hot-wall heat flux values by modeling the thermal response of the TPS subject to iteratively-refined entry heating profiles [5]. Integration of IHT-based results into CFD-based cold-wall correction schemes and Kalman filter-based sensor fusion methodologies—combining measurements from total heat flux sensors, radiometers, and thermocouple plugs via IHT—have also generated better agreement of predicted and measured entry heat flux values [2,7]. IHT-based methods, however, are characteristically ill-posed, and susceptible to large instabilities if the input temperature measurement contains small errors or noise. Regularization techniques, such as Tikhonov regularization or truncated singular value decomposition, can be used to damp the amplification of measurement errors; however, doing so often incurs a tradeoff between solution noise and the retention of sharp features [8]. These drawbacks to current CFD- and IHT-based methods motivate the development of more efficient and robust algorithms to recover TPS hot-wall heat flux values directly from on-board instrumentation.

This work details the development of a Green's function sensor fusion approach to recover hot-wall TPS heat flux values from embedded heat flux sensor and temperature measurement instrumentation. Green's functions have been leveraged in the aerothermodynamics community to efficiently model heat conduction in complex systems [9–12]. Non-linear adaptations of the Green's function formulation in systems where the effects from temperature-dependent material properties are significant [9,11] have also demonstrated the approach as a viable candidate to model the thermal response of common TPS materials. Most significantly, the Green's function formalism allows for collocated heat flux and temperature measurements to be integrated into a single solution formulation, providing an efficient platform to directly reconstruct hot-wall heat flux values solely from measurement inputs. Furthermore, the integration of the heat flux sensor in the problem formulation allows for the use of a measurement surrogate to stabilize the IHT-generated solution, leading to a more robust regularization mechanism with fewer tradeoffs compared to conventional methods.

The remainder of this paper is organized as follows. The Green's function approach used to recover TPS surface heat flux values from collocated heat flux and temperature measurements (herein referred to as the *hot-wall heat flux reconstruction algorithm*) is presented in Section III. In Sections IV.A and IV.B, the hot-wall heat flux reconstruction algorithm is evaluated on 1D and 3D axisymmetric model systems, respectively. The sensitivity of the algorithm to varying input parameters is analyzed, and its robustness to noisy input measurements is compared against a conventional IHT regularization approach.

III. Hot-Wall Heat Flux Reconstruction Algorithm

A schematic of the heat flux sensor (HFS) and surrounding TPS (herein referred to as the *TPS-sensor system*) is shown in Fig. 1. During transient heating scenarios, the disparate thermal properties between the heat flux sensor and the TPS drives a large divergence between the surface temperatures of each component; while the surface of the insulating TPS becomes hot, the heat flux sensor surface remains cold, close to initial conditions. As a result, a difference arises in the net heat flux absorbed into the heat flux sensor and TPS through various heat transfer mechanisms, such as convection and radiative dissipation.
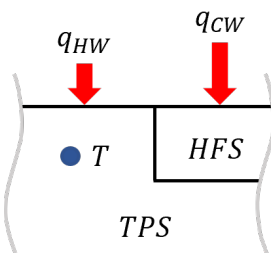

Fig. 1 Schematic of the TPS-sensor system. The heat flux absorbed by the cold-wall heat flux sensor q_{CW} is augmented compared to the heat flux absorbed by the hot-wall TPS q_{HW}. Temperature probes are embedded within the TPS near the heat flux sensor to obtain discrete temperature measurements.

Applied to the TPS-sensor system, the reconstruction framework aims to recover the hot-wall heat flux absorbed into the TPS (q_{HW}) using the time history of the cold-wall heat flux (q_{CW}), measured by the heat flux sensor, and temperature measurements from sensors embedded in the surrounding TPS. The reconstruction approach consists of two main technical steps. First the TPS-sensor system is modeled using Green's functions to establish a relationship between the hot- and cold-wall heat flux boundary conditions and the subsurface temperature distribution. When the

thermal properties of the components are temperature-dependent, an additional step precedes the formulation of Green's function to linearize the heat conduction equation. Second, the Green's function representation of the TPS-sensor system is inverted to recover the hot-wall TPS heat flux, leveraging the heat flux sensor measurement to stabilize the solution.

A. Nonlinear Heat Conduction

The temperature distribution within a solid is governed by the heat conduction equation

$$\rho C_p(\tilde{T})\frac{\partial \tilde{T}}{\partial t} = \nabla \cdot \left[k(\tilde{T})\nabla \tilde{T}\right] + g(\boldsymbol{x}, t) \tag{1}$$

To model the heat transfer in a system with temperature-dependent material properties using Green's functions, Eq. (1) must be linearized. To eliminate nonlinear terms produced by expansion of the divergence operator in Eq. (1), a Cole-Hopf transform $T = f(\theta)$ is employed, where T represents the temperature change from an initial reference temperature $T = \tilde{T} - \tilde{T}_0$. Following [13], the Cole-Hopf transformation $f(\theta)$ is the solution to the following homogeneous differential equation

$$\frac{d}{d\theta}\left[k(f)\frac{df}{d\theta}\right] = 0 \tag{2}$$

such that Eq. (1) may be recast as

$$\frac{1}{\alpha(f)}\frac{\partial \theta}{\partial t} = \nabla^2\theta + \frac{g(\boldsymbol{x}, t)}{A} \tag{3}$$

where A is an integration constant from the solution of Eq. (2), to be defined for each material separately. To further linearize Eq. (3), $\alpha(f)$ is separated into constant and temperature-dependent components [13,14]

$$\alpha(f) = \alpha_0 + \alpha_T(f) \tag{4}$$

where α_0 is the thermal diffusivity at the reference temperature $\tilde{T}_0$ and $\alpha_T(f)$ is a general function of temperature relative to $\tilde{T}_0$. Substituting Eq. (4) into Eq. (3) and simplifying yields

$$\frac{1}{\alpha_0}\frac{\partial \theta}{\partial t} - \nabla^2\theta = \frac{\alpha_T(f)}{\alpha_0}\nabla^2\theta + \frac{\alpha(f)}{\alpha_0}\frac{g(\boldsymbol{x}, t)}{A} \tag{5}$$

noting that the right-hand side of Eq. (5) may be collapsed into a single energy generation term g'/A

$$\frac{g'(\boldsymbol{x}, t)}{A} = \frac{\alpha_T(f)}{\alpha_0}\nabla^2\theta + \frac{\alpha(f)}{\alpha_0}\frac{g(\boldsymbol{x}, t)}{A} \tag{6}$$

Eq. (5) is now reduced to a linearized expression of the heat conduction equation

$$\frac{1}{\alpha_0}\frac{\partial \theta}{\partial t} - \nabla^2\theta = \frac{g'(\boldsymbol{x}, t)}{A} \tag{7}$$

where the effects of temperature-dependent material properties are captured by the inhomogeneous source term. When the material properties are temperature-dependent, $\theta = T$, $A = k$, and g' reduces to g.

B. Green's Function Representation of the TPS-Sensor System

Green's function models the impulse response of a linear system and is applied to the heat conduction problem via an analogous auxiliary equation [15]

$$\frac{1}{\alpha_0}\frac{\partial G}{\partial t} - \nabla^2 G = \frac{1}{\alpha_0}\delta(\boldsymbol{x} - \boldsymbol{x_0}, t - \tau) \tag{8}$$

Equation (8) models Green's function $G(\boldsymbol{x}, t, \boldsymbol{x_0}, \tau)$ as the response to a Dirac delta heat pulse $\delta(\boldsymbol{x} - \boldsymbol{x_0}, t - \tau)$ occurring at location $\boldsymbol{x_0}$ and time τ. Combining Eq. (7) and Eq. (8), rearranging terms, and integrating over the domain volume, as per [15], leads to an integral representation of the transformed temperature distribution subject to time-dependent boundary conditions

$$
\begin{aligned}
\theta(\boldsymbol{x}, t) = & \int_V \theta(\boldsymbol{x_0}, 0)G(\boldsymbol{x}, t, \boldsymbol{x_0}, 0)\ dV_0 \\
& + \int_0^t \int_V \frac{\alpha_0}{A} g'(\boldsymbol{x_0}, \tau)G(\boldsymbol{x}, t, \boldsymbol{x_0}, \tau)\ dV_0\ d\tau \\
& + \int_0^t \int_S \alpha_0 \nabla_0\theta(\boldsymbol{x_0}, \tau)G(\boldsymbol{x}, t, \boldsymbol{x_0}, \tau)\cdot \hat{n}\ dS_0\ d\tau \\
& - \int_0^t \int_S \alpha_0\theta(\boldsymbol{x_0}, \tau)\nabla_0 G(\boldsymbol{x}, t, \boldsymbol{x_0}, \tau)\cdot \hat{n}\ dS_0\ d\tau
\end{aligned}
\tag{9}
$$

In Eq. (9), the first volume integral represents the effects of initial conditions. The second volume integral captures the effects of temperature-dependent material properties and internal heat sources. The third integral accounts for the effects of Neumann boundary conditions acting on the external boundaries of the domain. The last integral term in Eq. (9) accounts for Dirichlet boundary conditions.

Within the Cole-Hopf transformation, Fourier's law relates the gradient of θ normal to the system boundary with the absorbed heat flux into the solid q via [13]

$$q = -A\nabla\theta \cdot \hat{n} \tag{10}$$

and allows the third integral term in Eq. (9) to be expressed as a function of q

$$-\int_0^t \int_S \frac{\alpha_0}{A} q(\boldsymbol{x_0}, \tau)G(\boldsymbol{x}, t, \boldsymbol{x_0}, \tau)\ dS_0\ d\tau \tag{11}$$

Because the only inhomogeneous boundary condition in the TPS-sensor system is captured by the third term in Eq. (9) and the initial conditions are zero by definition of $T = \tilde{T} - \tilde{T}_0$, the first and last integral terms in Eq. (9) vanish. Expanding the remaining volume and surface integrals to separate the heat flux sensor and TPS domains, the transformed temperature distribution within the TPS can be modeled via

$$
\begin{aligned}
\theta(\boldsymbol{x}, t) = & -\int_0^t \int_{S_{TPS}} \frac{\alpha_{0,TPS}}{A_{TPS}} q_{HW}(\tau)G_{TPS,TPS}(\boldsymbol{x}, t, \boldsymbol{x_0}, \tau)\ dS_0\ d\tau \\
& -\int_0^t \int_{S_{HFS}} \frac{\alpha_{0,HFS}}{A_{HFS}} q_{CW}(\tau)G_{TPS,HFS}(\boldsymbol{x}, t, \boldsymbol{x_0}, \tau)\ dS_0\ d\tau \\
& +\int_0^t \int_{V_{TPS}} \frac{\alpha_{0,TPS}}{A_{TPS}} g'_{TPS}(\boldsymbol{x_0}, \tau)G_{TPS,TPS}(\boldsymbol{x}, t, \boldsymbol{x_0}, \tau)\ dV_0\ d\tau \\
& +\int_0^t \int_{V_{HFS}} \frac{\alpha_{0,HFS}}{A_{HFS}} g'_{HFS}(\boldsymbol{x_0}, \tau)G_{TPS,HFS}(\boldsymbol{x}, t, \boldsymbol{x_0}, \tau)\ dV_0\ d\tau
\end{aligned}
\tag{12}
$$

The surface integral terms on the right-hand side of Eq. (12) represent individual contributions of q_{HW} and q_{CW} on the transformed temperature rise measured within the TPS. The additional volume integral terms capture the effects of the temperature-dependence of the material properties within each domain on the transformed temperature rise in the TPS. G represents the Green's function of the TPS due to a heat flux boundary condition or source term imposed on the TPS $\left(G_{TPS,TPS}\right)$ or on the heat flux sensor $\left(G_{TPS,HFS}\right)$. In the hot-wall heat flux reconstruction framework, Green's functions are constructed for the TPS-sensor system using the Galerkin method to approximate the linear heat conduction eigenfunctions ϕ_n. Adapted from [9,15],

5

$$G_{l,m}(\boldsymbol{x}, t, \boldsymbol{x_0}, \tau) = \sum_{n=1}^{N} \frac{k_{0,m}}{\alpha_{0,m}} \phi_n^{(l)}(\boldsymbol{x}) \phi_n^{(m)}(\boldsymbol{x_0}) e^{-\Lambda_{n,n}(t-\tau)} \qquad l, m = TPS \text{ or } HFS \qquad (13)$$

where the eigenfunctions are expressed as an N-ordered sum of scaled basis functions χ_j

$$\phi_n^{(l)} = \sum_{j=1}^{N} \psi_{j,n} \chi_j^{(l)} \qquad l = TPS \text{ or } HFS \qquad (14)$$

In Eq. (13), the temperature-of-interest is located in domain l and the heat flux boundary condition or heat source is imposed on domain m. The variable $\Lambda_{n,n}$ represents the eigenvalue accompanying each eigenfunction ϕ_n. In Eq. (14), basis functions χ_j are required to satisfy the homogeneous boundary conditions imposed on the system and are defined separately for each domain. These basis functions are then scaled by the eigenvector ψ_n accompanying the respective eigenfunction ϕ_n. Eigenvalues $\Lambda_{n,n}$ and eigenvectors ψ_n are solved using the approach described in [11].

C. Recovery of the Hot-Wall TPS Heat Flux

In the second step of the reconstruction algorithm, the hot-wall heat flux is recovered from the Green's function representation of the TPS-sensor system. The hot-wall heat flux is first isolated from all other quantities in Eq. (12). For tractability, measured quantities are combined into a single parameter $\gamma(\boldsymbol{x}, t)$

$$\gamma(\boldsymbol{x}, t) = \theta(\boldsymbol{x}, t) + \int_0^t \int_{S_{HFS}} \frac{\alpha_{0,HFS}}{A_{HFS}} q_{CW}(\tau) G_{TPS,HFS}(\boldsymbol{x}, t, \boldsymbol{x_0}, \tau) \, dS_0 \, d\tau \qquad (15)$$

Likewise, the source terms which capture the effects of temperature-dependent material properties are collapsed into a separate parameter $\epsilon(\boldsymbol{x}, t)$

$$\begin{aligned}
\epsilon(x, t) = &\int_0^t \int_{V_{HFS}} \frac{\alpha_{0,HFS}}{A_{HFS}} g'_{HFS}(\boldsymbol{x_0}, \tau) G_{TPS,HFS}(x, t, x_0, \tau) \, dV_0 \, d\tau \\
&+ \int_0^t \int_{V_{TPS}} \frac{\alpha_{0,TPS}}{A_{TPS}} g'_{TPS}(\boldsymbol{x_0}, \tau) G_{TPS,TPS}(x, t, x_0, \tau) \, dV_0 \, d\tau
\end{aligned} \qquad (16)$$

It should be noted that, because g' is an implicit function of $\nabla^2 \theta$, ϵ must be calculated simultaneously with q_{HW}. Eq. (12) can then be expressed as

$$\gamma(\boldsymbol{x}, t) - \epsilon(\boldsymbol{x}, t) = -\int_0^t \int_{S_{TPS}} \frac{\alpha_{0,TPS}}{A_{TPS}} q_{HW}(\tau) G_{TPS,TPS}(\boldsymbol{x}, t, \boldsymbol{x_0}, \tau) \, dS_0 \, d\tau \qquad (17)$$

Eq. (17) explicitly defines the relationship between measured quantities, nonlinear sub-surface effects, and the unknown hot-wall heat flux. Because heat flux and temperature measurements are sampled at a finite rate of $1/\Delta t$, Eq. (17) is recast as a discrete linear system [12]

$$\{\gamma\} - \{\epsilon\} = -\frac{\alpha_{0,TPS}}{A_{TPS}} [G]\{q_{HW}\} \qquad (18)$$

In Eq. (18), for N_s measurement samples, γ is now represented as an $N_s - 1 \times 1$ vector, discarding the temperature measurement at $t = 0$, and Green's function becomes an $N_s - 1 \times N_s - 1$ lower triangle matrix where each element represents an incremental integration of Green's function

$$G_{i,j} = \int_{t_{j-1}}^{t_j} \int_{S_{TPS}} G(\boldsymbol{x}, t_i, \boldsymbol{x_0}, \tau) \, dS_0 \, d\tau \qquad (19)$$

To mitigate the amplification of measurement noise present in γ, inversion of Eq. (18) requires solution regularization [8,12,16–18]. Typically, regularization is implemented by minimizing a penalty function of q_{HW}. In conventional regularization techniques, e.g., Tikhonov regularization, the solution of Eq. (18) seeks to simultaneously minimize the squared l^2-norms of the measurement residual and the squared l^2-norm of the solution [8], such that

$$\min\left\{\left\|\{\gamma\} - \{\epsilon\} + \frac{\alpha_{0,TPS}}{A_{TPS}}[G]\{q_{HW}\}\right\|_2^2 + \|\lambda q_{HW}\|_2^2\right\} \tag{20}$$

where λ tunes the strength of the penalty function embedded in the second l^2-norm. While an effective mechanism to damp noise-induced measurement instabilities, this method requires optimization of regularization parameters for each application and leads to a tradeoff between the resolution of sharp features in the heat flux and solution stability (see Sections IV.A2 and IV.B2) [8,12,19]. In the reconstruction framework described herein, the cold-wall heat flux sensor is used instead as a measurement surrogate to regularize the solution by enforcing smoothness between the hot- and cold-wall heat flux time histories

$$q_{HW} = C(t)q_{CW} + C_0(t)\bar{q}_{CW} \tag{21}$$

where $C(t)$ is an unknown, smooth, time-varying function with a continuous 2nd derivative in time. An additional time-dependent coefficient $C_0(t)$ is incorporated in Eq. (21) to avoid singularities that occur in $C(t)$ when the ratio q_{CW}/q_{HW} is small. These singularities may develop in pulsed heating scenarios or when the TPS-sensor system is subject to discontinuous boundary conditions. The coefficient $C_0(t)$ scales the quantity $\bar{q}_{CW}$, which represents the average value of q_{CW} up to time $t + \tau_{HFS}$, where τ_{HFS} is the response time of the heat flux sensor. Additional details regarding the effects of singularities on the reconstruction algorithm and the impact of $C_0(t)$ in Eq. (21) are included in the appendix. In discretized form, $C(t)$ and $C_0(t)$ are two $N_s - 1$ length vectors to-be-determined

$$q_{HW} = [diag(q_{CW})\ diag(\bar{q}_{CW})]\begin{Bmatrix} C \\ C_0 \end{Bmatrix} \tag{22}$$

where $diag(q_{CW})$ and $diag(\bar{q}_{CW})$ are square matrices with q_{CW} and $\bar{q}_{CW}$, respectively, arranged along the diagonal elements. Eq. (18) is then recast as a function of C and C_0, yielding

$$\{\gamma\} - \{\epsilon\} = -\frac{\alpha_{0,TPS}}{A_{TPS}}[G][diag(q_{CW})\ diag(\bar{q}_{CW})]\begin{Bmatrix} C \\ C_0 \end{Bmatrix} \tag{23}$$

The regularized solution of C and C_0 aims to simultaneously minimize the squared l^2-norms of the measurement residual and the 2nd derivatives of C and C_0, in effect enforcing smoothness in C and C_0. The minimization statement can be expressed explicitly as

$$\min\left\{\left\|\{\gamma\} - \{\epsilon\} + \frac{\alpha_{0,TPS}}{A_{TPS}}[G]\ [diag(q_{CW})\ diag(\bar{q}_{CW})]\begin{Bmatrix} C \\ C_0 \end{Bmatrix}\right\|_2^2 + \left\|\begin{Bmatrix} \lambda_2 \\ \lambda_2^{(0)} \end{Bmatrix} \cdot \begin{bmatrix} L_2 \\ L_2 \end{bmatrix}\begin{Bmatrix} C \\ C_0 \end{Bmatrix}\right\|_2^2\right\} \tag{24}$$

In Eq. (24) the regularization coefficients λ_2 and $\lambda_2^{(0)}$ are introduced to tune the magnitude of the 2nd derivative penalty term, where L_2 is a discrete 2nd derivative finite difference operator acting on C and C_0. The coefficient $\lambda_2^{(0)}$ is defined relative to λ_2, such that λ_2 remains the sole user-input parameter in Eq. (24).

$$\lambda_2^{(0)} = C_\lambda \lambda_2 \tag{25}$$

Finally, it is important to emphasize that the minimization statement in Eq. (24) may be calculated directly without requiring the use of time marching or optimization schemes. Even in scenarios where temperature-dependent effects are present, Eq. (24) may be calculated simultaneously with Eq. (16), a well-posed operation, to reach an accurate solution. The efficiency of the hot-wall heat flux reconstruction algorithm also positions it well for computationally expensive parametric analyses, such as stochastic uncertainty quantification, which may be resource limited when using time-marching methods.

IV. Results

A. Verification of the Reconstruction Algorithm using a 1D Test Case

A computational verification test case was constructed to analyze the accuracy of the reconstruction algorithm and evaluate its sensitivity to varying input parameters. The verification test case models a one-dimensional linear system with constant material properties subject to step heat flux boundary conditions [12]. A schematic of the 1D test case is shown in Fig. 2. A rod (labeled TPS) of thickness $L = 10\ mm$, thermal conductivity $k = 0.05\ W/m \cdot K$, and thermal diffusivity $\alpha = 2 \times 10^{-7}\ m^2/s$, representative of SLA-561 at -73°C [20], is embedded into a perfectly insulating housing adjacent to, but thermally isolated from, a heat flux sensor. The rod has an initial temperature of $\tilde{T}_0$ and is exposed to a step heat flux $q_{HW} = 1\ kW/m^2$ at $x = L$ and $t = t_0$. The rod is held at a constant temperature of $\tilde{T}_0$ at $x = 0$. The heat flux sensor is exposed to the same step heat flux profile, but with a larger amplitude of $q_{CW} = 1.5 \times q_{HW}$ to simulate a cold-wall boundary condition. A temperature probe is embedded in the rod at $x = x_T$.
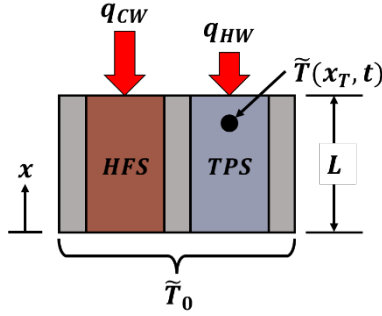
Fig. 2 Schematic of the 1D verification test case. A 1D rod (labeled TPS) is exposed to a step heat flux and the temperature response is measured by a temperature probe at x_T. The face at $x = 0$ is held at a constant temperature $\tilde{T}_0$. A collocated heat flux sensor (labeled HFS) measures an augmented heat flux step.

The temperature probe measurement is simulated using an analytical solution to the transient heat conduction problem. The heat flux sensor measurement q_{HFS} is simulated with a first order exponential rise to q_{CW} with a time constant of τ_{HFS}

$$q_{HFS} = q_{CW}[1 - \exp(-t/\tau_{HFS})] \tag{26}$$

In the reconstruction algorithm (Section III), q_{HFS} is used in place of q_{CW} to simulate the application of the algorithm in a measurement scenario with a finite-rate heat flux sensor response. Temperature and heat flux measurement inputs are shown in Fig. 3 for multiple temperature probe positions x_T and heat flux sensor response times τ_{HFS}, calculated up to 20 seconds after initiation of the step. Unless otherwise noted, a heat flux sensor response time of $\tau_{HFS} = 0.2s$ was used in all reconstructions.
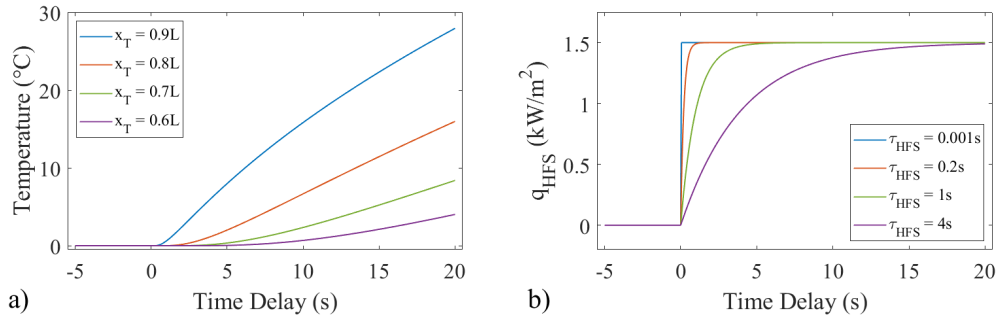

Fig. 3 Hot-wall heat flux reconstruction algorithm inputs in the 1D test case. a) Simulated temperature probe measurements. b) Simulated heat flux sensor measurements.

In the reconstruction algorithm, Green's function is approximated using an N-order set of monomial basis functions [9]

8

$$\chi_j = x^j \tag{27}$$

The heat flux absorbed by the rod at $x = L$ was recovered using the reconstruction algorithm described in Section III and compared with the imposed step heat flux boundary condition. The algorithm was tested using various measurement (x_T, τ_{HFS}) and reconstruction (N, λ_2) parameters. The quality of the reconstruction was quantified by calculating the root-mean-squared-error (RMSE) of the reconstructed heat flux profile

$$\text{RMSE} = \sqrt{\frac{1}{length(q_{HW})} \sum_{i=1}^{length(q_{HW})} \left[q_{HW}^{(i)} - q_{HW,ref}^{(i)}\right]^2} \tag{28}$$

where q_{HW} is the reconstructed heat flux profile and $q_{HW,ref}$ is the exact heat flux profile imposed on the surface of the rod. In all scenarios, RMSE values were calculated for the duration of the measurement beginning 2s after the heat flux step, excluding fluctuations near the step region.

1. Reconstruction Algorithm Convergence

First, the accuracy and convergence of the reconstruction algorithm is investigated as a function of measurement, material, and system parameters. In the following analysis, temperature and heat flux measurements are sampled at a rate of 20 Hz. To damp out oscillations near the step region caused by the finite rate heat flux sensor response (relative to the instantaneous cold-wall heat flux step) a regularization coefficient of $\lambda_2 = 10^4$ was used to stabilize the reconstruction.

Figure 4 shows a family of reconstructed heat flux profiles of varying basis function order for two locations of the temperature probe measurement, $x_T = 0.7L$ (Fig. 4a) and $x_T = 0.9L$ (Fig. 4b). Notably, the speed of convergence varies significantly depending on where the temperature measurement is sampled in the solid. Close to the surface, the algorithm converges within only a few basis function terms, while deep into the structure, a larger basis function order is required to recover the step heat flux profile satisfactorily.
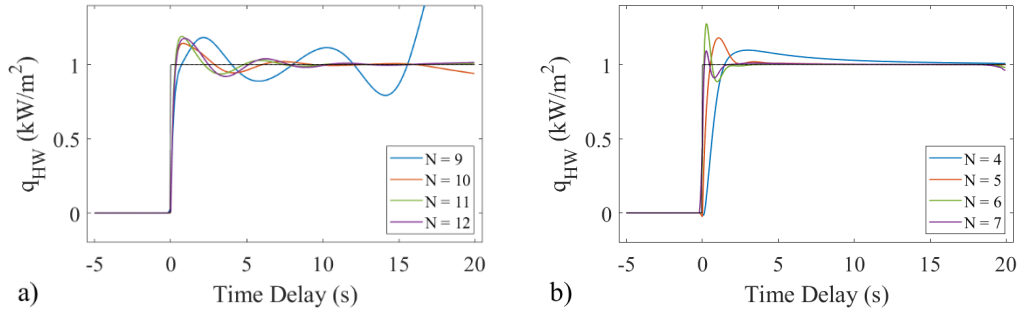

Fig. 4 Reconstructed heat flux profiles using a temperature measurement from a) $x_T = 0.7L$ and b) $x_T = 0.9L$ for various basis function orders.

To generalize regions of convergence as a function of system parameters, a parametric sweep was performed by simultaneously varying the basis function order $3 \leq N \leq 15$, temperature measurement location $0.6L \leq x_T \leq 0.9L$, and measurement duration $5s \leq t_m \leq 45s$. The sweep was repeated for two additional thermal diffusivity values, $\alpha = 4.5 \times 10^{-7} \ m^2/s$ and $\alpha = 1 \times 10^{-6} \ m^2/s$, to sample a wide range of system response times. RMSE values are plotted in Fig. 5a as a function of the dimensionless parameter $\alpha t_m/(L - x_T)^2$, typically referred to as the dimensionless thermal penetration depth [12] or diffusion number, and the basis function order N.

In Fig. 5a, a notable region of reconstructed hot-wall heat flux profiles with RMSE values of less than $25 \ W/m^2$ (2.5% of full-scale q_{HW}) appears in the upper right-hand portion. The boundary of this region can be approximated by a line superimposed in Fig. 5a with the equation

$$\log_{10}\left[\frac{\alpha t_m}{(L - x_T)^2}\right] + \frac{N}{20} = 0.25 \tag{29}$$
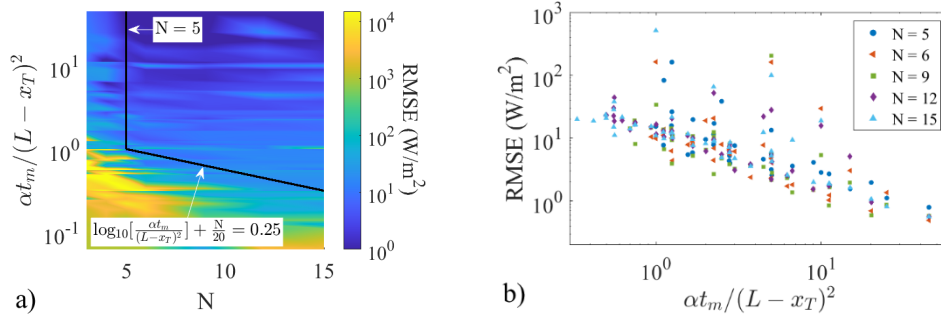
9

Fig. 5 Parametric analysis of hot-wall heat flux reconstruction convergence in the 1D test case. a) Colored heatmap of the RMSE of reconstructed hot-wall heat flux profiles as a function of measurement and reconstruction algorithm parameters. Note the logarithmic color scale and y-axis. The black boundary denotes a region in the upper right portion in which the RMSE is less than $25\,W/m^2$ (2.5% of full-scale q_{HW}). b) RMSE results as a function of the diffusion number for datapoints sampled from the upper right portion of Fig. 5a. Each data series corresponds to a constant basis function order.

for all $N \geq 5$. Within this region, increasing the accuracy of the reconstruction algorithm becomes dependent on increasing the value of the parameter $\alpha t_m/(L - x_T)^2$, with diminishing or no improvements observed from increasing the basis function order (Fig. 5b). These bounds given by Eq. (29) can be used to determine the minimum value of N required to adequately reconstruct hot-wall surface heat flux values given a pre-defined value of $\alpha t_m/(L - x_T)^2$. Applied to the 1D model system for a measurement duration of $20s$, the reconstruction algorithm is projected to generate accurate results when using a basis function order of $N \geq 12$ and $N \geq 5$ for a temperature probe placed at $x = 0.7L$ and $x_T = 0.9L$, respectively, in good agreement with the results shown in Fig. 4.

2. Reconstruction Algorithm Stability

The purpose of the regularization coefficient is to tune the damping of amplified measurement noise and stabilize the inversion of Green's function. In conventional spectral regularization techniques, such as Tikhonov regularization, the value of the regularization coefficient λ which provides high quality solutions is often confined to a very narrow region [8]. Because these techniques penalize certain features of the solution directly, sub-optimal values of λ may either obscure solution features with significant oscillations or remove sharp features entirely. In contrast, the hot-wall heat flux reconstruction algorithm insulates the reconstructed solution from adverse regularization effects by instead penalizing non-smooth behavior in the ratio q_{HW}/q_{CW}. Physically, this penalty is justified due to the finite rate at which the surface temperatures of the heat flux sensor and TPS develop towards cold- and hot-wall conditions. In this section, the impacts of both regularization methods on the reconstructed hot-wall heat flux are analyzed and compared.

In the following series of tests, reconstructed hot-wall heat flux profiles were calculated using a range of λ_2 values spanning from $\lambda_2 = 4 \times 10^5$ to $\lambda_2 = 2 \times 10^8$. $\lambda_2^{(0)}$ was defined as a large multiple of λ_2

$$\lambda_2^{(0)} = 10^3 \times \lambda_2 \tag{30}$$

In each scenario, the temperature measurement was sampled from $x_T = 0.8L$. A basis function order of $N = 10$ was used to construct Green's function. To simulate errors in the measurements, three levels of gaussian noise were added directly to the input measurements (Fig. 6). Noise parameters are tabulated in Table 1, where σ_T and σ_{HFS} represent the standard deviations of the noise applied to the temperature probe and heat flux sensor measurements, respectively. Each measurement was sampled at a rate of 100 Hz (2500 total measurement points) to achieve reproducible noise distributions for all reconstructions. RMSE values were calculated for each level of input measurement noise and value of λ_2. This calculation was repeated 50 times using independently generated noise inputs for each sweep to produce a range of RMSE values.

Results of the parametric sweeps of λ_2 are shown in Fig. 7a for all three noise levels. Individual datapoints represent the mean RMSE values from the 50 repeat sweeps per measurement noise level, with the shaded regions enveloping two standard deviations of calculated RMSE values for all sweeps. In the hot-wall heat flux reconstruction algorithm, the effect of increasing λ_2 from small values is a gradual increase in the accuracy and stability of the reconstruction (Fig. 7a). At regularization coefficient values of approximately $\lambda_2 = 3 \times 10^6$ and $\lambda_2 = 5 \times 10^6$, RMSE values become insensitive to variations in the regularization coefficient for the low/medium and high input

measurement noise scenarios, respectively. The reconstruction accuracy remains high as the regularization coefficient is increased to a value of $\lambda_2 = 4 \times 10^7$, with all mean RMSE values falling below $105\ W/m^2$ (10.5% full-scale heat flux).

Table 1. Input temperature and heat flux sensor measurement noise parameters.

Noise Level	$\sigma_T\ (°C)$	$\sigma_{HES}\ (W/m^2)$
Low	$0.1 + 0.025 \times (\tilde{T} - \tilde{T}_0)$	37.5
Medium	$0.2 + 0.05 \times (\tilde{T} - \tilde{T}_0)$	75
High	$0.4 + 0.1 \times (\tilde{T} - \tilde{T}_0)$	150
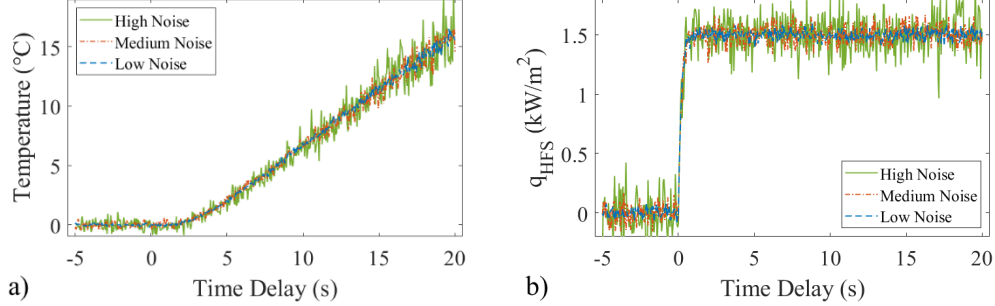
Fig. 6 Measurement inputs with added noise, plotted at 20 Hz. a) Examples of temperature probe measurements. b) Examples of heat flux sensor measurements.

The stratification of RMSE values by input measurement noise level is the result of the smooth coupling between q_{HW} and q_{CW}, via the heat flux sensor measurement (Eq. (21)); while the reconstructed solution is stable, noise from the heat flux sensor measurement proportional to q_{HW}/q_{CW} is propagated into the reconstruction. As such, the uncertainty of the reconstructed hot-wall heat flux profile due to the input heat flux sensor measurement can be expected to be linear to the uncertainty of the input heat flux sensor measurement itself. Finally, increasing the regularization coefficient beyond $\lambda_2 = 4 \times 10^7$ leads to a sharp increase in the reconstruction error for all levels of measurement noise, indicating that the solution has become overregularized.
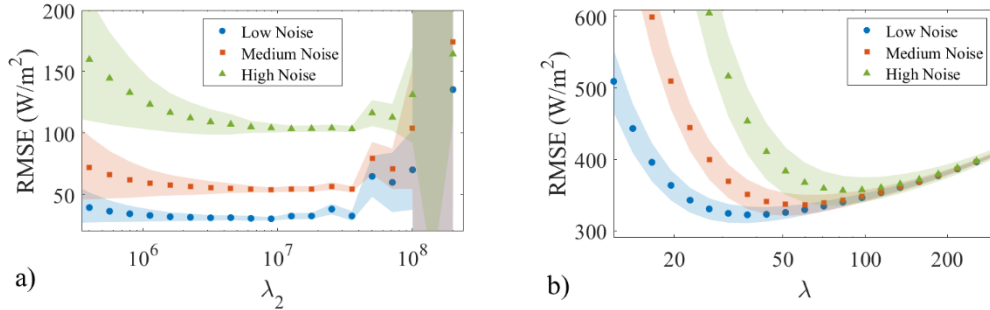

Fig. 7 RMSE values for low, medium, and high noise measurement inputs as a function of the regularization coefficient using a) the hot-wall heat flux reconstruction algorithm and b) Tikhonov regularization.

Results from a parallel series of sweeps using the same temperature measurement inputs (Fig. 6a), but stabilized using Tikhonov regularization, are presented in Fig. 7b. Increasing λ from small values leads to a sharp decrease in the RMSE of the reconstructed heat flux profile. RMSE values continue to decrease to a local minimum at separate locations for each level of input measurement noise before increasing thereafter. Minimal RMSE values occur for the low, medium, and high measurement noise levels with regularization coefficient values of $\lambda = 37,\ 60,$ and 90, respectively. With large values of λ, the reconstructed heat flux profiles coalesce towards the same RMSE values. In this region, all noise-induced instabilities have become damped, however increasing the value of λ results in over-smoothing of the step discontinuity and an increase in error at the edge of the reconstruction ($t - t_0 = 20s$).

A juxtaposition of the results shown in Fig. 7a and 7b illustrates the stability that may be achieved with a regularization surrogate. When using Tikhonov regularization (Fig. 7b), and, more broadly, conventional spectral

regularization techniques, the regularization coefficient must be tailored for each measurement condition to achieve optimal results. In contrast, when using the hot-wall heat flux reconstruction algorithm, optimal results may be accessed using a range of λ_2 spanning from $\lambda_2 = 5 \times 10^6$ to $\lambda_2 = 4 \times 10^7$ for all levels of measurement noise. This level of robustness alleviates the need to define an optimal value of λ_2 for each measurement case, as would be required when using conventional regularization techniques, and generalizes the reconstruction algorithm for many different measurement conditions.

To analyze the quality of the reconstructions in both approaches, reconstructed heat flux profiles using both the hot-wall heat flux reconstruction algorithm (Fig. 8) and Tikhonov regularization (Fig. 9) are presented using optimal values of λ_2 and λ, respectively, for each level of measurement noise. A value of $\lambda_2 = 10^7$ was used for the former approach for all levels of measurement noise.
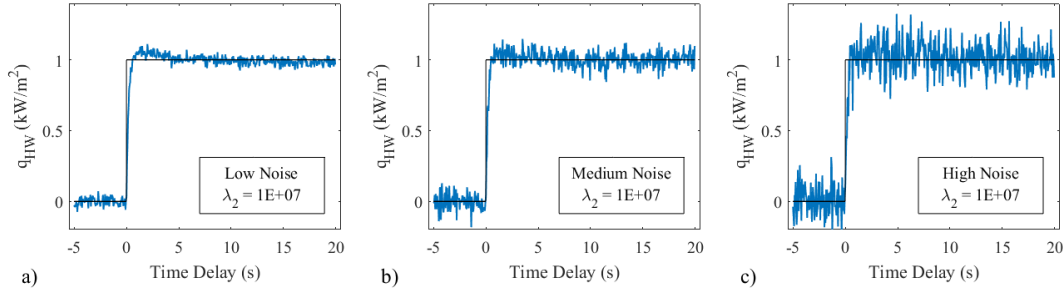
Fig. 8 Selected reconstructed heat flux profiles for different values of measurement input noise using the hot-wall heat flux reconstruction algorithm. An optimal regularization coefficient $\lambda_2 = 1 \times 10^7$ is used for all scenarios. a) Low noise. b) Medium noise. c) High noise. The data is plotted at a rate of 20 Hz.
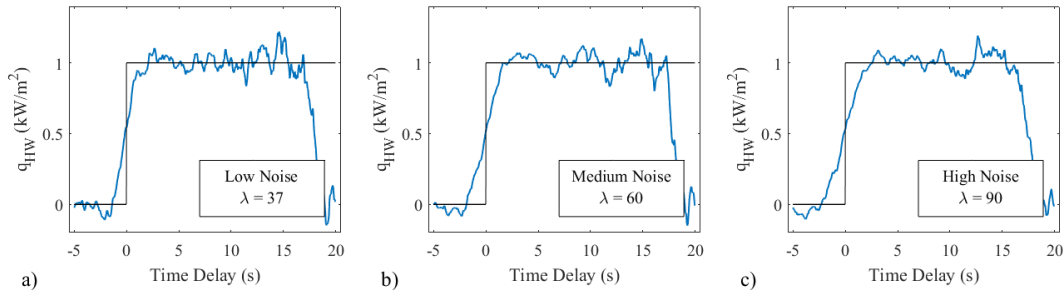

Fig. 9 Selected reconstructed heat flux profiles for different values of measurement input noise using Tikhonov regularization. Optimal regularization coefficients of $\lambda = 37, 60,$ and 90 were used for the a) Low noise, b) Medium noise, and c) High noise scenarios, respectively. The data is plotted at a rate of 20 Hz.

For all levels of measurement noise, the hot-wall heat flux reconstruction algorithm can resolve the step discontinuity at $t = t_0$ with minimal errors in the steady region of the heat flux profile (Fig. 8). Immediately following the step, a slight overshoot in the reconstruction is present due to the finite-rate heat flux sensor response. In each reconstruction, the level of noise increases commensurate with the level of input measurement noise; however, the solution remains stable for the entire step duration (Fig. 8).

Results for the reconstructed heat flux profiles using Tikhonov regularization (Fig. 9) illustrate the effects of increasing input measurement noise on the optimized solutions. While the instabilities are sufficiently damped in all scenarios, sharp features are lost near the step region. As the measurement input noise increases, the increasing value of λ that is required to produce optimal results induces significant over-smoothing near the step region. Furthermore, in all scenarios, the reconstructed heat flux profile near the end of the measurement $(t - t_0 > 15s)$ diverges from the steady state value.

B. 3D Axisymmetric Heat Pulse

To evaluate the performance of the hot-wall heat flux reconstruction algorithm in a more complex system, an axisymmetric model of the TPS-sensor system is analyzed subject to a convective heat pulse. A schematic of the model system is shown in Fig. 10. A heat flux sensor of radius $R_1 = 4\ mm$ is embedded in a TPS with outer radius of $R_2 = 16\ mm$ and a thickness of $L = 10\ mm$.
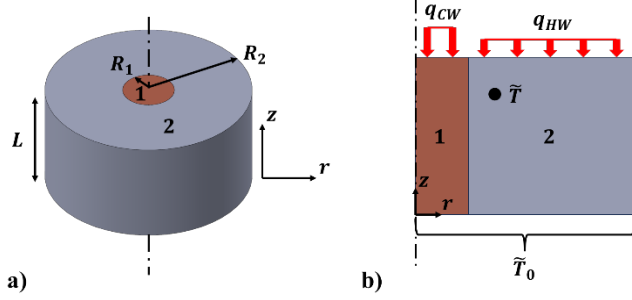
Fig. 10 3D axisymmetric model of the TPS-sensor system. The heat flux sensor is labeled as domain 1 and the TPS is labeled as domain 2. a) 3D isometric view of the model system. b) $r - z$ cross-section view of the model system. The top surface is exposed to a convective heat pulse. The bottom surface is held at a constant temperature $\tilde{T}_0$. Simulated heat flux and temperature measurements, q_{HFS} and $\tilde{T}$, respectively, are sampled from the finite element analysis heat conduction solution at $x_{HFS} = [0, 0.95L]$ and $x_T = [0.4R_2, 0.9L]$.

The heat flux sensor and TPS are modeled using temperature-dependent thermal properties representative of copper [21,22] and SLA-561 [20], respectively. In the reconstruction algorithm, the Cole-Hopf transformation is used to linearize the heat conduction equation when the material properties are temperature-dependent. A polynomial approximation is used to model the thermal conductivity of each material

$$k_l(T) = k_0 + k_{T,l}T + k_{TT,l}T^2 + \cdots \qquad l = HFS \text{ or } TPS \tag{31}$$

where k_0 is the thermal conductivity at the reference temperature $\tilde{T}_0$, and $k_T, k_{TT}, \ldots$ are higher order polynomial coefficients. Using Eq. (31) in Eq. (2), the transformed temperature becomes

$$\theta_l = \frac{1}{A_l}\left[k_{0,l}T + \frac{k_{T,l}T^2}{2} + \frac{k_{TT,l}T^3}{3} + \cdots\right] + B_l \tag{32}$$

In Eq. (32), A_l and B_l are derived from the boundary and interface conditions of the model, as detailed in the appendix. In the reconstruction algorithm, input temperature measurements are transformed via Eq. (32). In addition, a numerical solution of the inverse of Eq. (32) is used to calculate the variation of the thermal properties within the TPS-sensor system (Eq. (4)) to model the effects of temperature-dependent material properties in Eq. (24) (via Eq. (16)).

The model system has an initial temperature of $\tilde{T}_0 = -73°C$ and is exposed to a $40s$ duration sinusoidal convective heat pulse at t_0 through variation of the freestream temperature $\tilde{T}_\infty$ at the top surface (Fig. 11a). To simulate a boundary layer transition event, the convective heat transfer coefficient h undergoes a sharp increase (three-fold over $0.25s$) prior to the peak of the freestream temperature (Fig. 11b). The bottom surface of the model is maintained at the initial temperature $\tilde{T}_0$, such that the temperature rise T is equal to 0. The $r = R_2$ face is insulated, which can be interpreted as enforcing 1D heat flow through the TPS when sufficiently far away from the TPS-sensor interface. To construct Green's functions, a Galerkin basis function set which satisfies the boundary and interface conditions imposed on the TPS-sensor system was used, as detailed in the appendix.

To recover hot-wall heat flux values using the reconstruction algorithm, input temperature and heat flux measurements are generated from finite element analysis (FEA) simulations (Ansys Mechanical ™). The temperature measurement (Fig. 12a) is simulated using the FEA-generated nodal temperature solution located at $x_T = [0.4R_2, 0.9L]$. The heat flux sensor measurement q_{HFS} (Fig. 12b) is retrieved from the FEA-generated heat flux solution along the center axis of the model at $x_{HFS} = [0,0.95L]$. Both measurements are sampled at a rate of 8 Hz.

The heat flux sensor measurement is used directly to represent the cold-wall heat flux q_{CW} absorbed at the heat flux sensor surface. The location x_{HFS} is sufficiently close to the surface such that the lag between q_{HFS} and q_{CW} is governed by a time constant of $\sim 40\ ms$, far less than the interval between datapoints (see, for example, [23]).
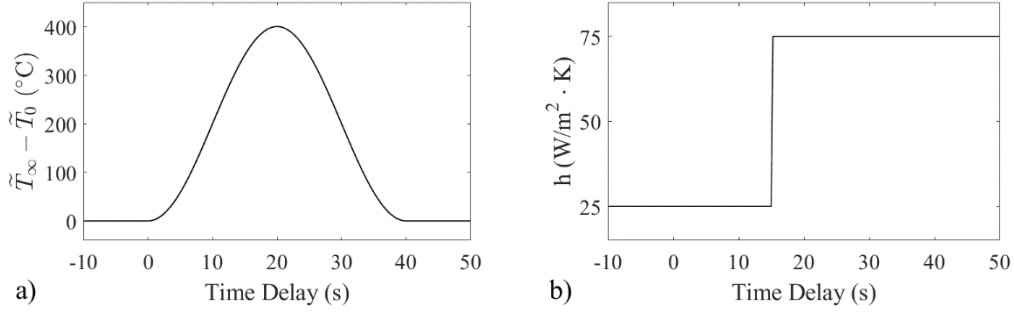
Fig. 11 Convective heat flux boundary conditions. a) Sinusoidal pulse of the freestream temperature relative to $\tilde{T}_0$. b) Convective heat transfer coefficient with sharp ramp at $t - t_0 = 15s$.
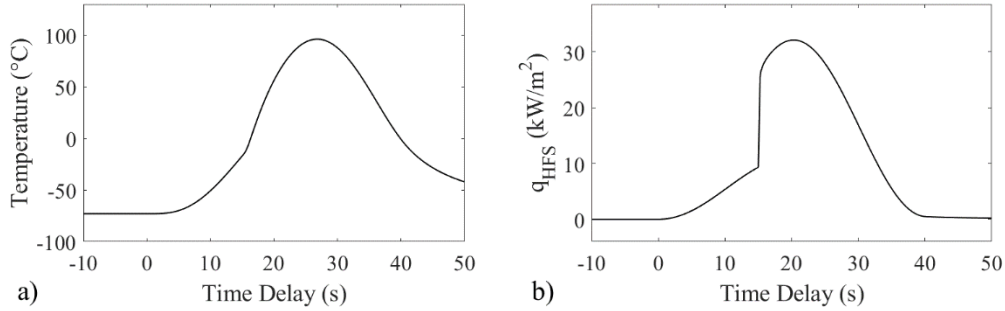

Fig. 12 FEA-generated measurement inputs for the 3D axisymmetric model system. a) Simulated temperature probe measurement. b) Simulated heat flux sensor measurement.

1. Verification of the Reconstruction Algorithm on the 3D Axisymmetric Model System

The hot-wall heat flux reconstruction algorithm is first evaluated on the 3D axisymmetric model system with noise-free measurement inputs. A basis function order of $M = 5$ and $N = 5$, corresponding to the radial and axial components, respectively, was used to construct Green's function. Regularization coefficient values of $\lambda_2 = 10^3$ and $\lambda_2^{(0)} = 10^3 \times \lambda_2$ were used to stabilize the solution.
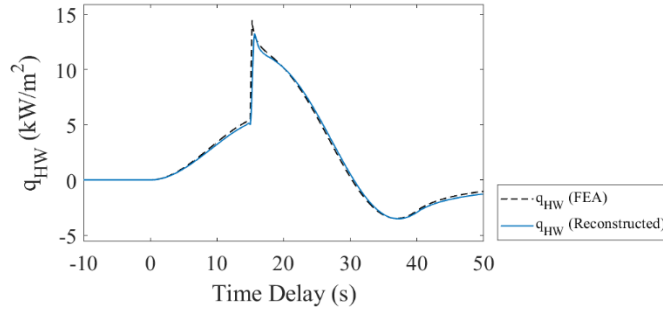

Fig. 13 Reconstructed hot-wall heat flux using noise-free input measurements (solid blue line). The dashed black line represents the FEA-generated TPS surface heat flux.

In the FEA-generated hot-wall heat flux profile, the increase in the heat transfer coefficient during the simulated boundary layer transition event at $t - t_0 = 15s$ introduces a proportional increase in the surface heat flux. Directly following the transition event, the TPS surface temperature increases rapidly towards the freestream temperature, reducing the magnitude of the heat flux. The heat flux continues to decrease following the peak in the freestream temperature (Fig. 11a) and changes sign as the freestream temperature falls below the TPS surface temperature.

In the reconstructed hot-wall heat flux profile, the sharp jump in heating during the simulated boundary layer transition event is resolved to within 9% of the FEA-generated value ($13.3 \ kW/m^2$ reconstructed (solid blue line) vs. $14.5 \ kW/m^2$ FEA (dashed black line)) with a delay of $0.375s$ in the temporal location of peak heating. Following

14

peak heating, and through the remainder of the heat pulse, the reconstruction algorithm closely predicts the FEA-generated hot-wall heat flux profile with a maximum error of $0.4\ kW/m^2$ at $t - t_0 = 16.75s$.

2. Robustness of the Reconstruction Algorithm

In Section IVA, the robustness of the reconstruction algorithm was demonstrated on a 1D model system subject to a step heat flux boundary condition. The sensitivity of the reconstructed hot-wall heat flux to varying measurement and user input parameters is now analyzed in the 3D axisymmetric model system. Measurement inputs were perturbed using three levels of noise (Fig. 14), tabulated in Table 2. Reconstructed hot-wall heat flux profiles were calculated using a range of regularization coefficient values spanning from $\lambda_2 = 10^6$ to $\lambda_2 = 2 \times 10^9$ for each level of measurement noise.

Table 2. Measurement noise input parameters for the 3D axisymmetric model system.

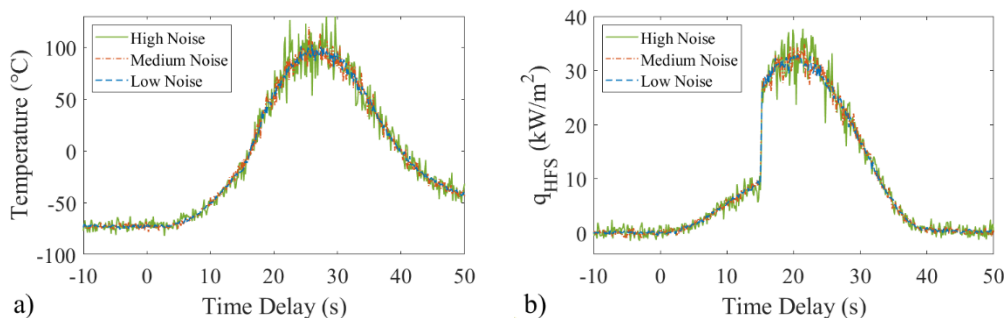| Noise Level	$\sigma_T\ (°C)$	$\sigma_{HFS}\ (kW/m^2)$
Low	$1 + 0.025 \times (\tilde{T} - \tilde{T}_0)$	$0.2 + 0.025 \times q_{HFS}$
Medium	$2 + 0.05 \times (\tilde{T} - \tilde{T}_0)$	$0.4 + 0.05 \times q_{HFS}$
High	$4 + 0.1 \times (\tilde{T} - \tilde{T}_0)$	$0.8 + 0.1 \times q_{HFS}$

Fig. 14 3D axisymmetric model system measurement inputs with added measurement noise. a) Examples of simulated temperature probe measurements. b) Examples of simulated heat flux sensor measurements.

In addition to the RMSE of the reconstruction (calculated for the entire measurement duration: $t - t_0 = -10s$ to $t - t_0 = 50s$), errors in the reconstructed peak heat flux and temporal location of peak heating were calculated for each value of input measurement noise and the regularization coefficient λ_2. All sweeps of λ_2 were repeated 50 times to generate a distribution of results and remove the influence of local noise fluctuations on the interpretation of the magnitude and temporal location of peak heating.

Consistent with the 1D results shown in Fig. 7a, the results from the axisymmetric model system outline a region of regularization coefficient values where the RMSE, peak heat flux error, and delay in the temporal location of peak heating are insensitive to variations in λ_2. This region of stability is bounded by approximately $\lambda_2 = 2 \times 10^7$ and $\lambda_2 = 2 \times 10^8$ for all levels of measurement noise (Fig. 15). Within these bounds, the peak heat flux error remains small, within $1\ kW/m^2$ on average (7% of peak heat flux) (Fig. 15b) and the temporal location of peak heating is predicted to within $2s$ for all levels of measurement noise (Fig. 15c), with larger variations in the high noise scenario compared to the low and medium noise scenarios. Beyond a value of $\lambda_2 = 2 \times 10^8$, an increase in the RMSE—caused in-part by an increase in the delay of the temporal location of peak heating, notably at $\lambda_2 = 3 \times 10^8$ (Fig. 15c)—and magnitude of the peak heating error (Figs. 15a and 15b) suggest that the solution has become over-regularized.

Results from the hot-wall heat flux reconstruction approach are compared next with results from a parallel series of sweeps using the same temperature measurement inputs (Fig. 14a), but stabilized using Tikhonov regularization (Fig. 16). Sweeps were performed using a range of regularization coefficient values spanning from $\lambda = 100$ to $\lambda = 2000$. In the reconstructed heat flux profiles, minimum RMSE values are optimized around a different regularization coefficient value for each level of input measurement noise, corresponding to $\lambda = 330, 450,$ and 700 for the low, medium, and high noise scenarios, respectively (Fig 16a). However, when only considering RMSE values for optimal results, significant errors emerge in the reconstructed peak heating value. At optimal values of λ, as per the minimum RMSE, the peak heat flux is underpredicted by $3\ kW/m^2$ at best (21% of peak heat flux), with a delay of at least $1.5s$ in the temporal location of peak heating (Figs. 16b and 16c).
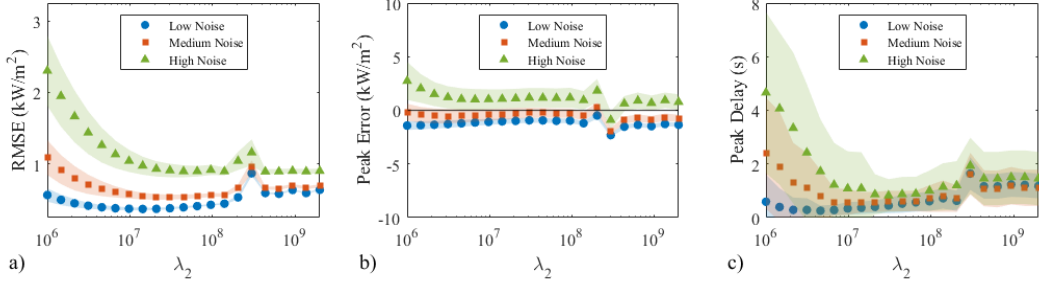
15

Fig. 15 Hot-wall heat flux reconstruction algorithm results from sweeps of λ_2 values. a) RMSE. b) Error in the magnitude of peak heating. c) Error in the temporal location of peak heating.
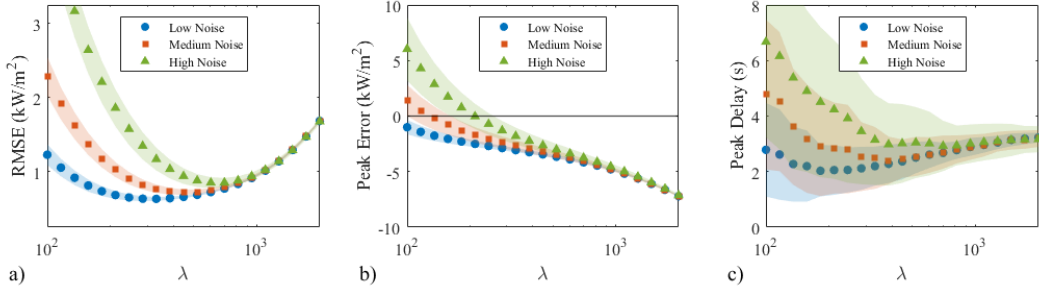

Fig. 16 Results from sweeps of λ values using Tikhonov regularization. a) RMSE. b) Error in the magnitude of peak heating. c) Error in the temporal location of peak heating.

To analyze the solution features from each reconstruction approach, Fig. 17 and Fig. 18 show families of reconstructed hot-wall heat flux profiles using the hot-wall heat flux reconstruction algorithm (Fig. 17) and Tikhonov regularization (Fig. 18). In each scenario, the average value of q_{HW} at each timestep (solid blue line) and the standard deviation of q_{HW} (blue shaded region) were calculated from the 50 repeat reconstructions. A regularization coefficient value of $\lambda_2 = 4 \times 10^7$ was used in the former approach for all input measurement noise levels (Fig. 17). Optimal regularization coefficient values, as per the minimum RMSE, were used in the Tikhonov regularization-based reconstructions (Fig. 18).

For all levels of input measurement noise, the hot-wall heat flux reconstruction algorithm can resolve the peak heat flux value to within 1.3 kW/m^2 (9% of peak heat flux) with a delay equal to or less than $0.375s$ in the temporal location of peak heating, on average (Fig. 17). Qualitatively, all mean reconstructed hot-wall heat flux profiles in Fig. 17 are similar. The effect of increasing the input measurement noise is an increase in the noise and variance of the reconstructed heat flux values, notably at, and directly following, the region of peak heating (Fig. 17c). This is primarily attributed to the increase in the heat flux sensor noise, as discussed in Section IVA. Prior to the sharp increase in heat flux at $t - t_0 = 15s$, a dip occurs in all reconstructed heat flux profiles. For large values of λ_2, which act to reduce the curvature in $C(t)$, features in q_{HW} that are not represented in q_{CW}, such as the sharp peak in the heat flux following the boundary layer transition event, may lead to reconstruction errors nearby in the time series. Yet, these errors do not have a demonstrable impact on other solution features, such as the sharp heating augmentation at $t - t_0 = 15s$ and smooth cool-down phase following $t - t_0 = 20s$, which are well-resolved in the reconstructed hot-wall heat flux profiles for all levels of input measurement noise (Fig. 17).

In contrast, the reconstructed hot-wall heat flux profiles using Tikhonov regularization further illustrate the drawbacks associated with spectral regularization methods. When the regularization coefficient is optimized around a minimum RMSE value, all sharp solution features are attenuated. At best, the peak heating value is underestimated by 3.2 kW/m^2 (22% of peak heat flux) with a $1.875s$ delay in the temporal location of peak heating (Fig. 18a). With an increase to the highest measurement noise level and the respective optimal regularization coefficient, the peak heating value is attenuated by up to 4 kW/m^2 (28% of peak heat flux) with a delay of $2.875s$ in the temporal location of peak heating (Fig. 18c).

Finally, it is worth noting that, while Tikhonov regularization is one of the most pervasive regularization techniques used in IHT problems, other novel regularization approaches are the subject of extensive research and may be better suited for resolving sharp features [17,24]. However, these approaches often involve assumptions of the

solution behavior a priori or the definition of extra regularization hyperparameters which need to be optimized for each measurement application. In contrast, the hot-wall heat flux reconstruction algorithm described herein only assumes that the relationship between the hot- and cold-wall heat flux values, driven by the evolution of the respective surface temperatures, varies at a finite rate. This physical justification lends the current approach to more general application to various measurement scenarios, with less guess work needed to obtain satisfactory results.
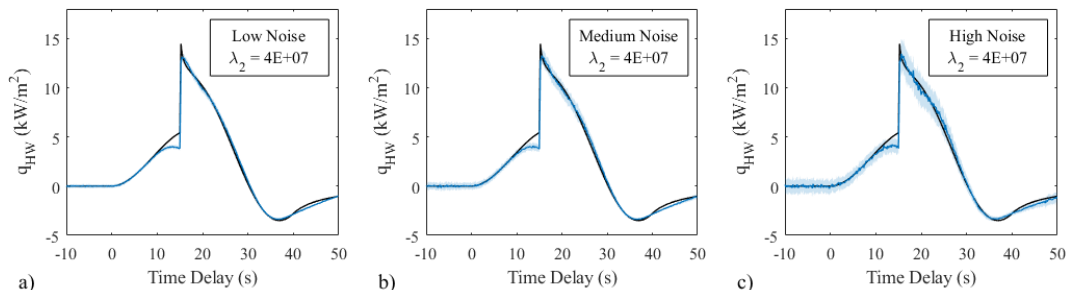

Fig. 17 Selected heat flux profiles reconstructed using the hot-wall heat flux reconstruction algorithm. a) Low noise. b) Medium noise. c) High noise.
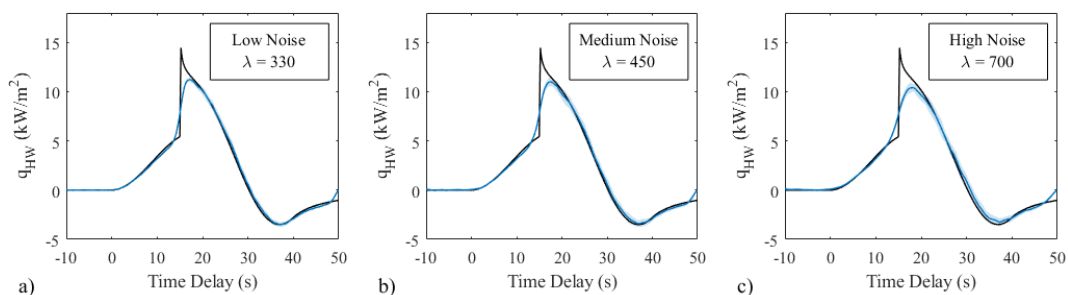

Fig. 18 Selected heat flux profiles reconstructed using Tikhonov regularization with optimal regularization coefficient values. a) Low noise. b) Medium noise. c) High noise.

V. Conclusion

A Green's function-based hot-wall heat flux reconstruction algorithm demonstrated an accurate computation of TPS surface heat flux values in 1D and 3D model systems solely using embedded thermal measurements. The algorithm leverages Green's functions to model the temperature measured within the TPS subject to hot- and cold-wall heat flux boundary conditions, and stabilizes the recovery of hot-wall heat flux values using the direct heat flux sensor as a surrogate regularization mechanism. The performance of the algorithm was evaluated on a 1D verification model subject to a step heat flux boundary condition. Analysis of the stability of the reconstruction algorithm subject to varying system parameters, such as temperature measurement location and duration, thermal properties of the conduction medium, and order of the Green's function basis, highlighted a broad region of algorithm convergence. For measurement scenarios with a diffusion number $\alpha t_m/(L - x_T)^2 \geq 1$, the algorithm can produce accurate results (RMSE of $< 2.5\%$ full-scale heat flux) with a 5-term approximation of Green's function. When subject to measurements perturbed with noise, the algorithm demonstrated a significant insensitivity to sub-optimal choice of the user input regularization parameter. Compared with the conventional Tikhonov regularization technique, the use of a surrogate measurement, i.e. the heat flux sensor, yielded accurate results for a much wider range of regularization coefficient values and demonstrated how the same regularization coefficient may be applied in different measurement conditions without a loss in solution quality. In a complex, nonlinear, 3D axisymmetric model system subject to a convective heating scenario, the algorithm can resolve sharp features and peak heating values following a simulated boundary layer transition event to within 9% of the FEA-generated reference value with a delay of $0.375 s$ in the reconstructed temporal location of peak heating. Subject to significant noise in the input measurements, the reconstruction algorithm demonstrated a substantial resilience to sub-optimal choice of the user input regularization coefficient, consistent with the 1D results. Compared with the Tikhonov regularization technique, the hot-wall heat flux reconstruction algorithm can resolve sharp transient heating features near the quickly varying peak heating region without introducing amplified measurement instabilities in areas with more slowly varying heat flux values. This

robustness positions the algorithm for use in a vast range of measurement applications without the need to optimize algorithm parameters for a specific end-use case, and more broadly demonstrates the viability of stabilizing ill-posed systems using surrogate measurements.

Appendix

Singularity Correction

In the reconstruction algorithm, the solution is stabilized by enforcing a smooth relationship between the measured cold-wall heat flux and the unknown hot-wall heat flux, i.e., $C(t)$. In Eq. (21), an additional unknown parameter $C_0(t)$ was introduced to correct for singularities which arise when the heat flux sensor measurement approaches zero. In the 3D axisymmetric model system described in Section IVB, this singularity arises after the heat pulse as the TPS surface temperature converges to the steady freestream temperature at a much slower rate than the heat flux sensor. Fig. 19 compares two reconstructed heat flux profiles with the singularity correction (Fig. 19a) and without the singularity correction (Fig. 19b), i.e., $C_0(t) = 0$, using low measurement noise inputs. Without the correction, the ratio q_{HW}/q_{CW} diverges to infinity as q_{CW} approaches zero at approximately $t - t_0 = 40s$. However, because large values of the 2nd derivative of $C(t)$ are penalized, minimization of the solution residual (the first l^2-norm in Eq. (24)) becomes favored, and instabilities develop in the reconstructed heat flux profile. Furthermore, as $C(t)$ becomes large, noise in the heat flux sensor measurement is amplified directly into the reconstructed hot-wall heat flux profile. The inclusion of the singularity correction allows the algorithm to revert to a temporary, but more stable, regularization mechanism to generate an accurate solution.
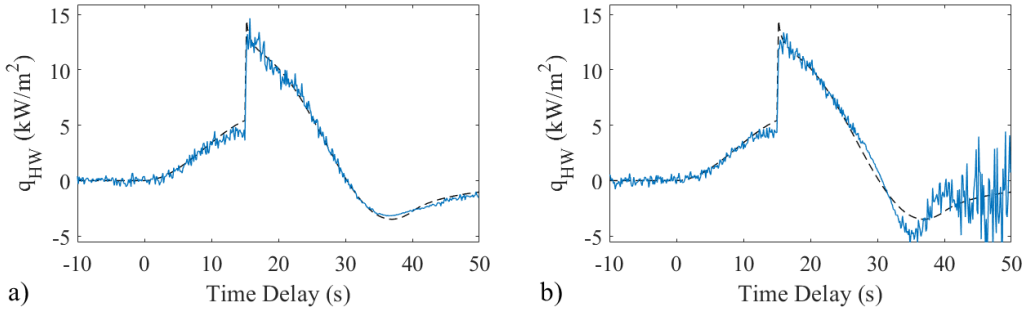

Fig. 19 Reconstructed hot-wall heat flux profiles a) with the singularity correction and b) without the singularity correction.

3D Axisymmetric Basis Functions

In the reconstruction algorithm, Green's function is approximated using a set of 3D axisymmetric basis functions which satisfy the homogeneous boundary conditions imposed on the system. These functions are first decomposed into components aligned along the orthogonal directions $\hat{r}$ and $\hat{z}$

$$\chi_j^{(l)}(r,z) = \mu_j^{(l)}(r)v_j^{(l)}(z) \qquad l = HFS \text{ or } TPS \tag{33}$$

In the TPS-sensor system, the following physical boundary and interface conditions must be satisfied

$$\left.\frac{\partial T_{HFS}}{\partial r}\right|_{r=0} = 0 \tag{34a}$$

$$\left.\frac{\partial T_{TPS}}{\partial r}\right|_{r=R_2} = 0 \tag{34b}$$

$$T_{HFS}|_{r=R_1} = T_{TPS}|_{r=R_1} \tag{34c}$$

$$k_{HFS}\left.\frac{\partial T_{HFS}}{\partial r}\right|_{r=R_1} = k_{TPS}\left.\frac{\partial T_{TPS}}{\partial r}\right|_{r=R_1} \tag{34d}$$

18

$$T_{HFS}|_{z=0} = T_{TPS}|_{z=0} = 0 \tag{34e}$$

Eq. (34a) enforces a smooth radial temperature distribution along the center axis within the heat flux sensor. Eq. (34b) enforces an adiabatic wall condition on the outer circumference of the TPS. Eq. (34c) and Eq. (34d) enforce continuity of temperature and heat flux across the shared TPS-sensor interface, respectively. Eq. (34e) enforces a homogeneous temperature boundary condition at $z = 0$.

Prior to constructing the basis functions, Eq. (34a-e) must be transformed via the Cole-Hopf transformation. To model the interface continuity condition, the thermal conductivity in each domain is first approximated with a linear temperature dependence

$$k_l'(T) = k_{0,l} + k_{T,l}'T \qquad l = HFS \text{ or } TPS \tag{35}$$

where $k_{0,l}$ is the thermal conductivity of domain l evaluated at the reference temperature $\tilde{T}_0$ and $k_{T,l}'$ approximates the linear variation of the thermal conductivity with respect to the reference temperature. Substituting the thermal conductivity profiles for each domain into Eq. (2) and integrating indefinitely yields the temperature transformation at the TPS-sensor interface

$$\theta_l' = \frac{1}{A_l}\left[k_{0,l}T + \frac{k_{T,l}'T^2}{2}\right] + B_l \tag{36}$$

where A_l and B_l are integration constants. Setting $B_l = 0$, such that the boundary condition defined by Eq. (34e) remains homogeneous, and $A_l = k_{0,l}^2/2k_{T,l}'$, the inverse transform becomes

$$T_l = \frac{k_{0,l}}{k_{T,l}'}\left[-1 + \sqrt{1 + \theta_l'}\right] \tag{37}$$

where the interface continuity condition $T_{HFS}(R_1, z) = T_{TPS}(R_1, z)$ can be expressed as

$$\frac{k_{0,HFS}}{k_{T,HFS}'}\left[-1 + \sqrt{1 + \theta_{HFS}'}\right]\Bigg|_{r=R_1} = \frac{k_{0,TPS}}{k_{T,TPS}'}\left[-1 + \sqrt{1 + \theta_{TPS}'}\right]\Bigg|_{r=R_1} \tag{38}$$

Expanding the $\sqrt{1 + \theta'}$ terms in Eq. (39) and ignoring higher order terms, the transformed interface continuity condition reduces to

$$\frac{k_{0,HFS}}{k_{T,HFS}'}\frac{\theta_{HFS}'}{2}\Bigg|_{r=R_1} = \frac{k_{0,TPS}}{k_{T,TPS}'}\frac{\theta_{TPS}'}{2}\Bigg|_{r=R_1} \tag{39}$$

Enforcing continuity of heat flux over the domain interface can be expressed directly using Eq. (10)

$$A_{HFS}\nabla\theta_{HFS}' \cdot \hat{n}_{HFS} = -A_{TPS}\nabla\theta_{TPS}' \cdot \hat{n}_{TPS} \tag{40}$$

It should be noted that, while A_l was chosen specifically to simplify the inverse transform in Eq. (37), scaling may be applied to the general Cole-Hopf transformation in Eq. (32) to increase the accuracy of the reconstruction. Using the mean value of the temperature probe measurement $\bar{T}$, θ is scaled such that

$$\frac{\theta_l(\bar{T})}{\theta_l'(\bar{T})} = 1 \tag{41}$$

The transformed physical boundary and interface conditions of the TPS-sensor system are thus satisfied with the following constraints applied to the basis functions:

$$\frac{\partial}{\partial r}\mu_j^{(HFS)}\bigg|_{r=0} = 0 \tag{42a}$$

$$\frac{\partial}{\partial r}\mu_j^{(TPS)}\bigg|_{r=R_2} = 0 \tag{42b}$$

$$\frac{k_{0,HFS}}{k'_{T,HFS}}\mu_j^{(HFS)}\bigg|_{r=R_1} = \frac{k_{0,TPS}}{k'_{T,TPS}}\mu_j^{(TPS)}\bigg|_{r=R_1} \tag{42c}$$

$$A_{HFS}\frac{\partial}{\partial r}\mu_j^{(HFS)}\bigg|_{r=R_1} = A_{TPS}\frac{\partial}{\partial r}\mu_j^{(TPS)}\bigg|_{r=R_1} \tag{42d}$$

$$v_j^{(HFS)}\bigg|_{z=0} = v_j^{(TPS)}\bigg|_{z=0} = 0 \tag{42e}$$

The axial boundary conditions Eq. (42e) are satisfied using a monomial basis function set [9].

$$v_j^{(HFS)} = v_j^{(TPS)} = z^{\xi_j} \tag{43}$$

where ξ is a set of integers up to order N. The radial interface conditions may be satisfied by recasting $\mu_j^{(HFS)}$ and $\mu_j^{(TPS)}$ in terms of a global basis function μ_j and perturbation μ'_j [15,25]

$$\mu_j^{(HFS)} = \mu_j \tag{44}$$

$$\mu_j^{(TPS)} = \frac{k_{0,HFS}}{k'_{T,HFS}}\frac{k'_{T,TPS}}{k_{0,TPS}}\mu_j + \Gamma\mu'_j \tag{45}$$

where μ'_j is designed to vanish at the $r = R_1$ interface and Γ is specified to satisfy Eq. (42d). In this formulation, the global basis function must satisfy both adiabatic constraints given by Eqs. (42a) and (42b) while the perturbation basis function must only satisfy the adiabatic constraint given by Eq. (42b). The global basis function is defined as a polynomial expression which contains derivatives with respect to r which vanish at $r = 0$ and $r = R_2$, adapted from [15]

$$\mu_j = \frac{(2\eta_j - 2)r^{2\eta_j}}{R_2^{2\eta_j-1}} - \frac{2\eta_j r^{2\eta_j-2}}{R_2^{2\eta_j-3}} \tag{46}$$

where η is a set of integers of order M specified to compliment the set ξ, such that all permutations of the elements of η and ξ are represented, e.g., $\eta = [1,2,3,1,2,3]$ and $\xi = [1,1,1,2,2,2]$. The perturbation basis function μ'_j must be designed to vanish at $r = R_1$, however its first derivatives must be non-zero for all terms at $r = R_1$ to maintain continuity of heat flux across the domain boundary (Eq. (42d)). These constraints, along with the adiabatic conditions at $r = R_2$, are satisfied with the following polynomial modified from [25]

$$\mu'_j = R_1 R_2 \eta_j \left[1 - \left(\frac{r}{R_1}\right)^{\eta_j+1}\right] - R_2^2(\eta_j + 1)\left[1 - \left(\frac{r}{R_1}\right)^{\eta_j}\right] \tag{47}$$

Substituting Eq. (46) and Eq. (47) into Eq. (44) and Eq. (45), differentiating with respect to r, and evaluating at the interface (Eq. (42d)) yields the definition of Γ

$$\Gamma = \frac{\left(\frac{A_{HFS}}{A_{TPS}} - \frac{k'_{T,TPS}}{k_{0,TPS}}\frac{k_{0,HFS}}{k'_{T,HFS}}\right)2\eta_j\left(2\eta_j - 2\right)\left(\frac{R_1}{R_2}\right)^{2\eta_J - 3}\left[\frac{R_1^2}{R_2^2} - 1\right]}{R_2\eta_j\left(\eta_j + 1\right)\left[\frac{R_2}{R_1} - 1\right]} \tag{48}$$

Acknowledgments

References

[1] Gülhan, A., Thiele, T., Siebe, F., Kronen, R., and Schleutker, T., "Aerothermal Measurements from the ExoMars Schiaparelli Capsule Entry," *Journal of Spacecraft and Rockets*, Vol. 56, No. 1, 2019, pp. 68–81. https://doi.org/10.2514/1.A34228

[2] Miller, R. A., Tang, C. Y., Santos, J. A. B., White, T. R., and Cruden, B. A., "Aftbody Heat Flux Measurements During Mars 2020 Entry," *Journal of Spacecraft and Rockets*, Vol. 61, No. 2, 2024, pp. 369–382. https://doi.org/10.2514/1.A35783

[3] Swanson, G., Kazemba, C., Miller, R. A., Alpert, H., Williams, J., Stephen, H., and Cheatwood, N., "Overview and Performance of the LOFTID Instrumentation Suite," presented at the AIAA SCITECH 2024 Forum, 2024. https://doi.org/10.2514/6.2024-1712

[4] Dutta, S., Braun, R. D., and Karlgaard, C. D., "Uncertainty Quantification for Mars Entry, Descent, and Landing Reconstruction Using Adaptive Filtering," *Journal of Spacecraft and Rockets*, Vol. 51, No. 3, 2014, pp. 967–977. https://doi.org/10.2514/1.A32716

[5] Alpert, H. S., Saunders, D. A., Mahzari, M., Monk, J. D., White, T. R., and West, T. K., "Inverse Estimation and Sensitivity Analysis of Mars 2020 Entry Aeroheating Environments," *Journal of Spacecraft and Rockets*, Vol. 60, No. 3, 2023, pp. 899–911. https://doi.org/10.2514/1.A35571

[6] Mahzari, M., Braun, R. D., White, T. R., and Bose, D., "Inverse Estimation of the Mars Science Laboratory Entry Aeroheating and Heatshield Response," *Journal of Spacecraft and Rockets*, Vol. 52, No. 4, 2015, pp. 1203–1216. https://doi.org/10.2514/1.A33053

[7] Stoffel, T. D., Karlgaard, C. D., White, T. R., and West, T. K., "Fusion of In-Flight Aerothermodynamic Heating Sensor Measurements Using Kalman Filtering," *Journal of Spacecraft and Rockets*, Vol. 61, No. 2, 2024, pp. 599–610. https://doi.org/10.2514/1.A35641

[8] Hansen, P. C., "Deconvolution and Regularization with Toeplitz Matrices," *Numerical Algorithms*, Vol. 29, No. 4, 2002, pp. 323–378. https://doi.org/10.1023/A:1015222829062

[9] Massa, L., and Schetz, J. A., "Hypersonic Heat Flux Reconstruction with Distributed Temperature Sensors," *Journal of Thermophysics and Heat Transfer*, Vol. 34, No. 2, 2020, pp. 331–346. https://doi.org/10.2514/1.T5778

[10] Nguyen, N., Ruda, M., Massa, L., Adams, C., and Schetz, J., "High Frequency, Multidimensional Heat Flux Reconstruction in Hypersonic Wind Tunnels," presented at the AIAA AVIATION 2020 FORUM, VIRTUAL EVENT, 2020. https://doi.org/10.2514/6.2020-3292

[11] Nguyen, N. M., Ruda, M. L., and Massa, L., "Effect of Insulations and Coatings on Hypersonic Heat Flux Reconstruction," *Journal of Thermophysics and Heat Transfer*, Vol. 35, No. 1, 2021, pp. 63–79. https://doi.org/10.2514/1.T5995

[12] Whalen, T. J., Laurence, S. J., Marineau, E. C., and Ozawa, H., "A Green's Function Approach to Heat-Flux Estimation from Temperature-Sensitive Paint Measurements," *Measurement Science and Technology*, Vol. 32, No. 11, 2021, p. 114011. https://doi.org/10.1088/1361-6501/ac16ee

[13] Vadasz, P., "Analytical Solution to Nonlinear Thermal Diffusion: Kirchhoff Versus Cole–Hopf Transformations," *Journal of Heat Transfer*, Vol. 132, No. 12, 2010, p. 121302. https://doi.org/10.1115/1.4002325

[14] Bialecki, R., and Nowak, A. J., "Boundary Value Problems in Heat Conduction with Nonlinear Material and Nonlinear Boundary Conditions," *Applied Mathematical Modelling*, Vol. 5, No. 6, 1981, pp. 417–421. https://doi.org/10.1016/S0307-904X(81)80024-8

[15] Cole, K., Beck, J., Haji-Sheikh, A., and Litkouhi, B., "Heat Conduction Using Greens Functions," CRC Press, 2010.

[16] Beck, J. V., Blackwell, B., and Haji-Sheikh, A., "Comparison of Some Inverse Heat Conduction Methods Using Experimental Data," *International Journal of Heat and Mass Transfer*, Vol. 39, No. 17, 1996, pp. 3649–3657. https://doi.org/10.1016/0017-9310(96)00034-8

[17] Gholami, A., and Hosseini, S. M., "A Balanced Combination of Tikhonov and Total Variation Regularizations for Reconstruction of Piecewise-Smooth Signals," *Signal Processing*, Vol. 93, No. 7, 2013, pp. 1945–1960. https://doi.org/10.1016/j.sigpro.2012.12.008

[18] Nguyen, N., and Massa, L., "Regularization of the Hypersonic Heat Flux," presented at the AIAA SCITECH 2023 Forum, National Harbor, MD & Online, 2023. https://doi.org/10.2514/6.2023-1728

[19] Hansen, P. C., and O'Leary, D. P., "The Use of the L-Curve in the Regularization of Discrete Ill-Posed Problems," *SIAM Journal on Scientific Computing*, Vol. 14, No. 6, 1993, pp. 1487–1503. https://doi.org/10.1137/0914086

[20] Smyly, E. D., and Pears, C. D., "Properties of Ablation and Insulation Materials, Volume I: Thermal Properties of Some Filled and Foamed Low-Density Ablators," NAS1-7732–1, 1971.

[21] Ho, C. Y., Powell, R. W., and Liley, P. E., "Thermal Conductivity of the Elements," *Journal of Physical and Chemical Reference Data*, Vol. 1, No. 2, 1972, pp. 279–421. https://doi.org/10.1063/1.3253100

[22] MacDonald, R. A., and MacDonald, W. M., "Thermodynamic Properties of Fcc Metals at High Temperatures," *Physical Review B*, Vol. 24, No. 4, 1981, pp. 1715–1724. https://doi.org/10.1103/PhysRevB.24.1715

[23] Hager, N. E., Jr., "Thin Foil Heat Meter," *Review of Scientific Instruments*, Vol. 36, No. 11, 1965, pp. 1564–1570. https://doi.org/10.1063/1.1719394

[24] Han, J., and Lee, Y., "Inhomogeneous Regularization with Limited and Indirect Data," *Journal of Computational and Applied Mathematics*, Vol. 428, 2023, p. 115193. https://doi.org/10.1016/j.cam.2023.115193

[25] Haji-Sheikh, A., and Beck, J. V., "Green's Function Partitioning in Galerkin-Based Integral Solution of the Diffusion Equation," *Journal of Heat Transfer*, Vol. 112, No. 1, 1990, pp. 28–34. https://doi.org/10.1115/1.2910360